Available online at www.sciencedirect.com

SciVerse ScienceDirect

Ceramics International 39 (2013) 7331–7342

CERAMICS INTERNATIONAL

www.elsevier.com/locate/ceramint

Effect of zirconia content on the mechanosynthesis and structural features of fluorapatite-based composite nanopowders

Bahman Nasiri-Tabrizi*, Abbas Fahami

Materials Engineering Department, Najafabad Branch, Islamic Azad University, Najafabad, Isfahan, Iran

Received 12 January 2013; received in revised form 8 February 2013; accepted 21 February 2013
Available online 1 March 2013

Abstract

The influence of zirconia content on the mechanosynthesis of fluorapatite–zirconia composite nanopowders was investigated. The structural features of the specimens with different amounts of monoclinic zirconia (0–20 wt%) were examined after 5 h of mechanical activation. Results indicated that the formation of fluorapatite–zirconia composite was strongly influenced by the zirconia content. In the presence of 5–10 wt% monoclinic zirconia, fluorapatite–zirconia composite nanopowders were produced after 5 h of milling. With increasing zirconia content to 20 wt%, there was no trace of fluorapatite–zirconia composite. In the absence of zirconia, the average crystallite size, lattice strain and the volume fraction of grain boundary of fluorapatite were about 34 nm, 0.469% and 8.38%, respectively. These values reached 24 nm, 0.754% and 11.71% with the addition of 10 wt% monoclinic zirconia. In the presence of 10 wt% monoclinic zirconia, the fraction of crystalline phase considerably decreased after 5 h of milling. Results revealed that the lattice parameter deviations were affected by the zirconia content. Based on SEM observations, no significant differences in the size distribution and morphology of the agglomerates were observed.

Keywords: Zirconia content; Mechanosynthesis; Fluorapatite-based composite; Structural features

1. Introduction

Apatite is a group of crystalline minerals that can be represented by the formula $M_{10}(XO_4)_6Y_2$. In this formula, M can be replaced by a large number of different ions such as Ca^{2+}, Mg^{2+}, Sr^{2+}, Ba^{2+}, Mn^{2+}, Fe^{2+}, Zn^{2+}, Cd^{2+}, Pb^{2+}, H^+, Na^+, K^+, Al^{3+}, etc. Also, XO_4 can be substituted by PO_4^{3-}, AsO_4^{3-}, VO_4^{3-}, SO_4^{3-}, CO_3^{2-}, SiO_4^{3-}, etc. In the apatite formula, Y can be replaced by several anions for instance OH^-, F^-, Cl^-, Br^-, O^{2-}, and CO_4^{2-}. The most common apatite structure is called hydroxyapatite (HAp, $Ca_{10}(PO_4)_6(OH)_2$), where M, XO_4 and Y are Ca^{2+}, PO_4^{3-} and OH^-, respectively [1,2]. HAp seems to be the most appropriate ceramic material for artificial bone and tooth applications owing to its biological properties. Nonetheless, HAp has intrinsically high dissolution rate in a biological system, poor corrosion resistance in an acidic environment and poor chemical stability at high temperature [3,4]. One of the suitable methods for decreasing the dissolution rate is substitution of OH^{-1} groups in HAp by F^{-1} ions, which leads to the formation of fluorine-substituted hydroxyapatite (FHAp, $Ca_{10}(PO_4)_6(OH)_{2-x}F_x$). This ionic substitution causes an increase in crystallinity, a decrease in crystal strain, and an increase in thermal and chemical stability [5,6].

It has been found that the incorporation of bioinert ceramics into the calcium phosphates, improves the structural features as well as the mechanical properties. An ideal reinforcing material for the calcium phosphate-based composites has not yet been identified. As a result, several attempts have been made to develop HAp- and FHAp-based composites [7–19]. Zirconia (ZrO_2) is one of the most widely used reinforcing agents, due to its superb strength and fracture toughness [8–10]. However, special precautions need to be taken to avoid injurious reactions between apatite and ZrO_2 during the fabrication process [14]. It has been reported that HAp decomposed faster when the amount of ZrO_2 in the composites increased [15]. In addition, the high temperature decomposition of HAp was increased in the presence of cubic zirconia with MgO [16]. Therefore, the effect of

*Corresponding author. Tel.: +98 3114456551; fax: +98 3312291008.
E-mail address: bahman_nasiri@hotmail.com (B. Nasiri-Tabrizi).

0272-8842/$ - see front matter © 2013 Elsevier Ltd and Techna Group S.r.l. All rights reserved.
http://dx.doi.org/10.1016/j.ceramint.2013.02.072

addition of different reinforcing materials must be studied on the properties of calcium phosphate-based composites.

According to our recent studies [17,18], fluorapatite–zirconia (FAp–ZrO_2) composite nanopowders can be produced by solid state process. Results indicated that the formation of FAp–5%wt ZrO_2 composite nanopowders proceeded in several steps. Moreover, the annealing process led to the decomposition of FAp into tricalcium phosphate (β-TCP) and calcium fluoride (CaF_2), and to the transformation of monoclinic zirconia (m-ZrO_2) to the tetragonal form (t-ZrO_2). In this study, the influence of zirconia content on the characteristics of FAp–ZrO_2 composite nanopowders was investigated and the optimum composition was determined. Also, the average crystallite size, lattice strain, volume fraction of grain boundary, fraction of crystalline phase, lattice parameters and morphological features of the specimens were evaluated.

2. Materials and methods

The materials used in this research were calcium oxide (CaO, Merck), phosphorous pentoxide (P_2O_5, Merck), calcium fluoride (CaF_2, Merck) and monoclinic zirconia (m-ZrO_2, Merck). Mechanical activation was performed in a planetary ball mill using zirconia balls (20 mm in diameter) and sealed cylindrical polyamide-6 vials (vol. 125 ml). To evaluate the effect of ZrO_2 content on the formation of FAp–ZrO_2 composite nanopowders, different amounts of m-ZrO_2 (0, 5, 10, 15, 20 wt%) were mixed with CaO, P_2O_5, and CaF_2 according to reaction (1). In all experiments, the weight ratio of ball-to-powder, rotational speed and milling time were 20:1, 600 rpm and 5 h, respectively. Fig. 1 shows the influence of zirconia content on the mechanosynthesis of FAp–ZrO_2 composite nanopowders.

$$9CaO + 3P_2O_5 + CaF_2 + m\text{-}ZrO_2 \rightarrow Ca_{10}(PO_4)_6F_2 + m\text{-}ZrO_2 \quad (1)$$

The milled samples in the absence and presence of 5, 10, 15 and 20 wt% of m-ZrO_2 were named as 0ZFA, 5ZFA, 10ZFA, 15ZFA and 20ZFA, respectively. The specifications of the synthesis process and chemical composition of specimens are presented in Table 1.

Phase analysis of the experimental outcomes was performed by X-ray diffraction (Philips X-ray diffractometer (XRD), Cu-K_α radiation, 40 kV, 30 mA and 0.02 deg S^{-1} step scan). XRD graphs were recorded in the interval $20^\circ \le 2\theta \le 60^\circ$ at a scan speed of 1 deg/min. "*PANalytical X'Pert HighScore*" software was also used for the analysis of different peaks. The patterns were compared to the standards compiled by the Joint Committee on Powder Diffraction and Standards (JCPDS), which involved card #15-0876 for FAp, #037-1497 for CaO, #035-0816 for CaF_2, #01-1079 for $Ca(OH)_2$, #05-0318 for P_2O_5 and #037-1484 for m-ZrO_2. Crystallite size and lattice strain of the samples were determined by using the XRD data according to the following equations [19]:

$$D = \frac{K\lambda}{(b_{obs} - b_{std})(\cos\theta)} \quad (I)$$

$$E^2 = \frac{(b_{obs}^2 - b_{std}^2)}{(4\tan\theta)^2} \quad (II)$$

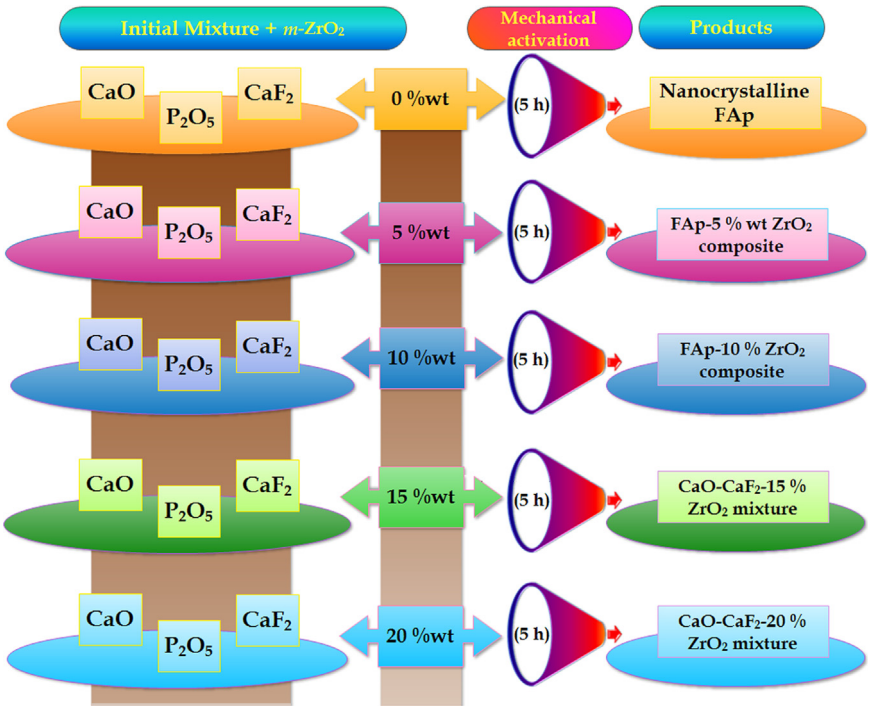

Fig. 1. The influence of m-ZrO_2 content on the mechanosynthesis of FAp–ZrO_2 composite nanopowders.

Table 1
Specifications of the synthesis process and chemical composition of specimens.

Series	Composition	Milling time (h)
0ZFA	100 wt% (CaO, P_2O_5, CaF_2)	5
5ZFA	95 wt% (CaO, P_2O_5, CaF_2)+5 wt% (m-ZrO_2)	5
10ZFA	90 wt% (CaO, P_2O_5, CaF_2)+10 wt% (m-ZrO_2)	5
15ZFA	85 wt% (CaO, P_2O_5, CaF_2)+15 wt% (m-ZrO_2)	5
20ZFA	80 wt% (CaO, P_2O_5, CaF_2)+20 wt% (m-ZrO_2)	5

where b (in radians), K, λ, D, E and θ are the structural broadening, shape coefficient (value between 0.9 and 1.0), the wavelength of the X-ray used (0.154056 nm), crystallite size, lattice strain and the Bragg angle (deg), respectively.

If we assume that a crystallite is a sphere of diameter D surrounded by a shell of grain boundary with thickness t, the volume fraction of grain boundary (f) is approximately [20]:

$$f = 1 - \left[\frac{D}{(D+t)}\right]^3 \quad \text{(III)}$$

The relation between lattice spacing (d) and lattice parameters (a, b, and c) of the hexagonal structures (FAp and the FAp in the composites) is shown as

$$\frac{1}{d^2} = \frac{4}{3}\frac{h^2+hk+k^2}{a^2} + \frac{l^2}{c^2} \quad \text{(IV)}$$

where h, k, l are the Miller indices of the reflection planes. The (002) and (300) reflections were chosen for the lattice parameters calculation [21].

Also, volume of fluorapatite HCP unit cell (V) was determined by the following formula [22]:

$$V = (3a^2c)(\sin 60^\circ) \quad \text{(V)}$$

The deviations of lattice parameters and unit cell volume (in terms of %) are shown as [23]

$$\text{Lattice parameter deviation} = \frac{\Delta x}{x_0}(x = a, c)(\%) \quad \text{(VI)}$$

$$\text{Unit cell volume deviation} = \frac{\Delta V}{V_0}(\%) \quad \text{(VII)}$$

where Δa, Δc and ΔV are defined as $\Delta a = a - a_0$, $\Delta c = c - c_0$ and $\Delta V = V - V_0$, respectively. Also, a_0, c_0 and V_0 are the standard values of FAp which equal to $a_0 = 9.368$ Å, $c_0 = 6.884$ Å and $V_0 = 1564.264$ Å^3.

The fraction of crystalline phase (crystallinity) was determined from the XRD data using the following equation [24]:

$$B_{hkl}\sqrt[3]{X_c} = \mathrm{K} \quad \text{(VIII)}$$

where X_c, K and B are the fraction of crystalline phase, a constant found equal to 0.24 and FWHM (deg) of selected reflection peaks, respectively. It should be mentioned that the structural features of the FAp were repeated two times for two groups of peaks; one group was (002), (211) and (300), and another was (222), (004) and (213) Miller's planes family. The average of these two measurements was presented as mean fraction of crystalline phase, crystallite size and lattice strain.

Fourier transform infrared (FT-IR, Model 680 Plus, JASCO) spectroscopy was also utilized to determine the functional groups of products. This spectroscopy was recorded in the range 4000–400 cm^{-1} at 2 cm^{-1} resolution by 16 scans. Energy dispersive X-ray spectroscopy (EDX) served as semi-quantitative examination of the samples (voltage used for EDX equal to 20 kV). Morphological features of the specimens were examined on a scanning electron microscope (SEM, SERON AIS-2100). In addition, a field emission scanning electron microscope (FE-SEM Hitachi S1831) that operated at the acceleration voltage of 15 kV was applied to appraise the volume fraction of grain boundary of the nanopowders by using the edge mode images.

3. Results and discussion

3.1. Phase evolution

Fig. 2 shows the XRD patterns of CaO, P_2O_5 and CaF_2 powder mixture in the absence and presence of different amounts of m-ZrO_2 (0–20 wt%) after mechanical activation for 5 h. As expected, phosphoric acid (H_3PO_4) formed immediately on addition of P_2O_5 to the reaction mixture due to very high hydrophilic nature of P_2O_5 (reaction (2)). Accordingly, characteristic peaks of P_2O_5 were not visible in XRD patterns.

$$3P_2O_5 + 9H_2O \rightarrow 6H_3PO_4, \qquad \Delta G_{298\,\mathrm{K}} = -493.081\ \mathrm{kJ}, \quad \Delta H_{298\,\mathrm{K}} = -586.317\ \mathrm{kJ} \quad (2)$$

In the absence of zirconia (0ZFA), all the peaks corresponding to the raw materials disappeared and only those belonging to FAp were detectable after 5 h of milling. By adding 5–10 wt% ZrO_2, FAp and m-ZrO_2 were obvious in XRD patterns of the milled samples. In fact, after 5 h of milling the main products of mechanochemical reactions for 5ZFA and 10ZFA samples were FAp–5 wt% ZrO_2 and FAp–10 wt% ZrO_2 composites, respectively. In these mechanochemical reactions, the extra peaks were not observed. This result confirmed the formation of FAp–ZrO_2 composites with high phase purity. According to Fig. 2, with increasing amount of zirconia up to 15 wt% (15ZFA), there was no trace of fluorapatite–zirconia composite. Similarly, in the presence

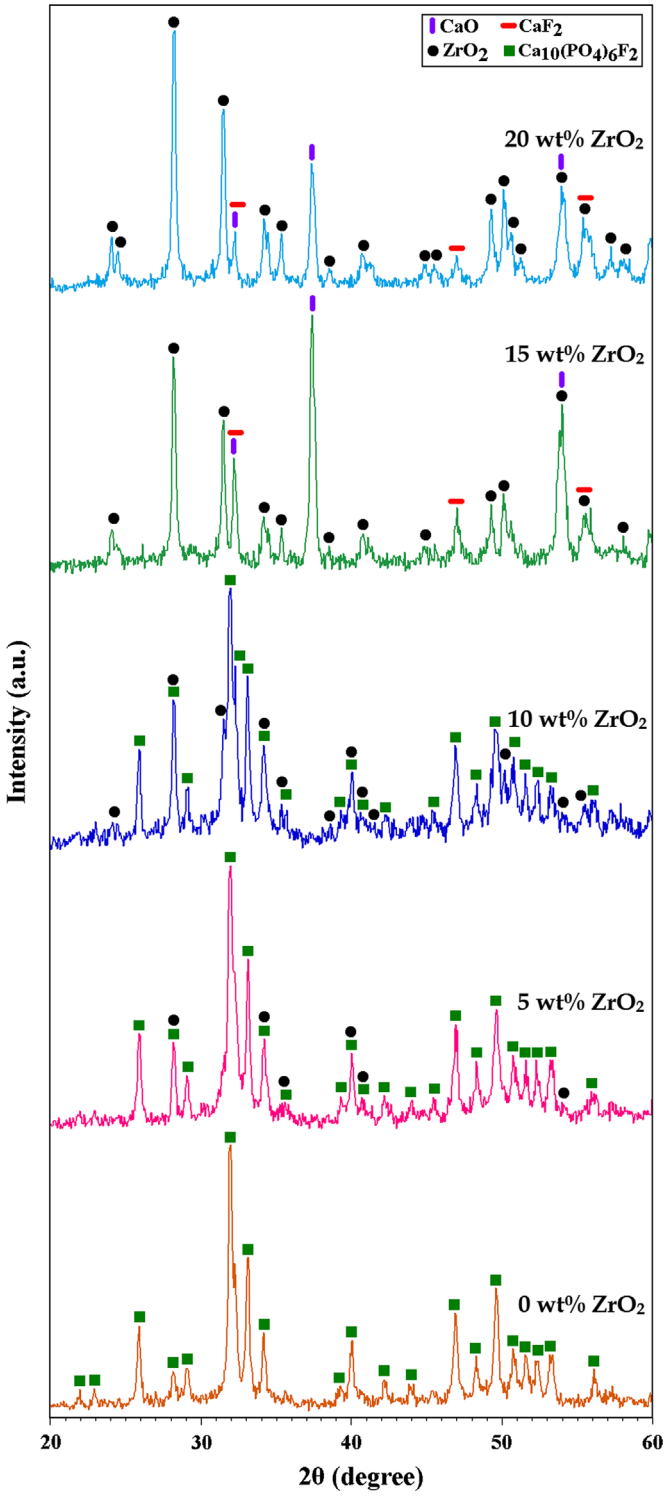

Fig. 2. XRD patterns of CaO, P_2O_5 and CaF_2 powder mixture in the absence and presence of different amounts of m-ZrO_2 (0–20 wt%) after mechanical activation for 5 h.

of 20 wt% ZrO_2 (20ZFA), the FAp–ZrO_2 composite was not detectable. For 15ZFA and 20ZFA samples, the phase compositions were CaF_2, CaO and m-ZrO_2. This effect can be attributed to the stoichiometric proportionality between the calcium and phosphorus reagents. In all experiments the total powder mass was 6 g. With increasing zirconia content to ≥ 15 wt%, the weight percent (wt%) of calcium and phosphorus sources including CaO, P_2O_5 and CaF_2 has diminished. It has been found that the formation of FAp–ZrO_2 composite by applying reaction (1) was affected by the stoichiometric proportionality between the calcium and phosphorus reagents [17,18]. Therefore, with decreasing weight percent of calcium and phosphorus sources, no mechanochemical reaction occurred after 5 h of milling due to the lack of required materials for mechanical activation. Nonetheless, after 5 h of mechanical activation only the reduction of particle size occurred. From the other point of view, as the ZrO_2 content was increased to ≥ 15 wt%, the reflection intensities of CaO and CaF_2 diminished and the peaks became wider, suggesting finer crystallite sizes and lattice micro-strains. Conversely, the reflection intensities of m-ZrO_2 increased. This behavior can be related to the dissolution of Ca ions in m-ZrO_2, and therefore the formation of a solid solution. Actually, in the presence of 15 and 20 wt% zirconia, the stabilization of m-ZrO_2 by calcium fluoride and calcium oxide as well as the formation of a solid solution of CaO–CaF_2–ZrO_2 occurred (reaction (3)).

$$\mathrm{CaO}\ [\mathrm{CaF_2}] + m\text{-}\mathrm{ZrO_2} \rightarrow \text{Ca-doped } m\text{-}\mathrm{ZrO_2} \quad (3)$$

Fig. 3a displays the magnified XRD region between $2\theta = 31^\circ$ and 35°. According to this figure, with increasing ZrO_2 content to 10 wt%, the reflection intensities of FAp decreased and the peaks became wider. This result suggests that with increasing zirconia content to 10 wt%, poorly crystalline structure was formed in comparison with 0ZFA sample. On the contrary, the reflections corresponding to ZrO_2 became more intense as the ZrO_2 content increased up to 10 wt%. Fig. 3b shows the magnified XRD region between $2\theta = 32.5^\circ$ and 33.5°. It can be seen that in the presence of 5 wt% zirconia, displacement of FAp peaks towards lower angles occurred after 5 h of milling. For 10ZFA, further displacement of FAp peaks was found (Fig. 3b). This indicates that the lattice parameter of FAp increases with the addition of zirconia due to an ion exchange reaction with ZrO^{2+} (0.21 nm) ions from the m-ZrO_2. It has been found that this reaction can occur where the surfaces of m-ZrO_2 and FAp are in contact, with minimum rearrangement of their structures [10].

3.2. Lattice parameters and their deviations

Unit cell measurements (a-axis, c-axis and unit cell volume (V)) of the FAp as a function of zirconia content were determined and the results of these are presented in Fig. 4. It is obvious that the a-axis and c-axis values for FAp in the 0ZFA and 5ZFA samples were similar to the reported values for standard FAp (#15-0876: $a = 9.368$ Å and $c = 6.884$ Å). However, these values were different from the standard FAp for 10ZFA sample (Fig. 4a). Results showed that the unit cell volume of FAp increased first in 0ZFA and then with the

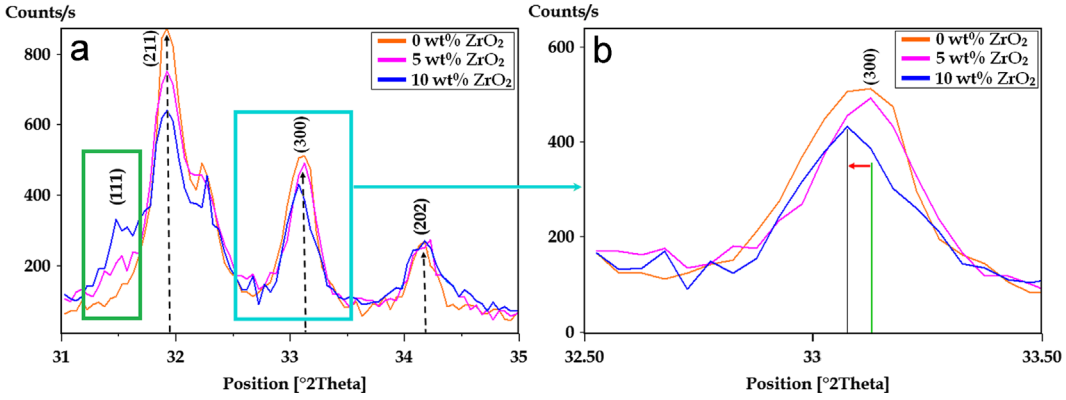

Fig. 3. Magnified XRD regions between (a) $2\theta = 31–35^\circ$ and (b) $2\theta = 32.5–33.5^\circ$.

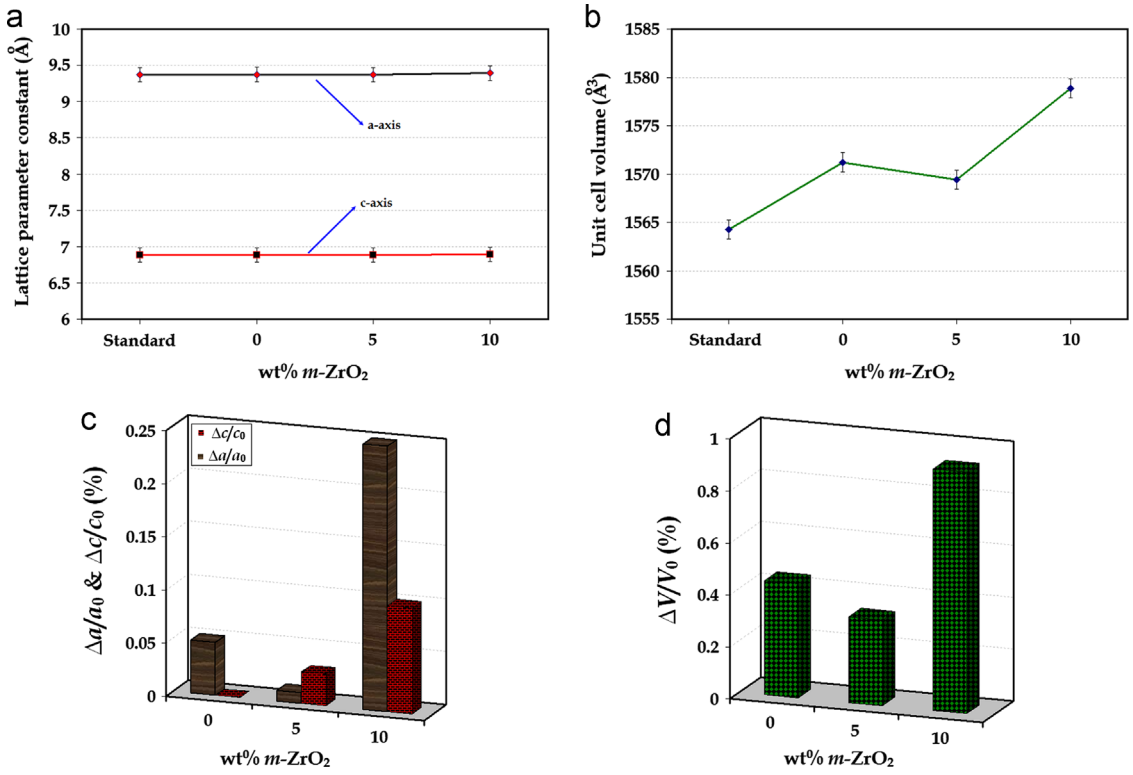

Fig. 4. Unit cell measurements (a) *a*-axis and *c*-axis, (b) unit cell volume, deviations of (c) lattice parameters and (d) unit cell volume of FAp as a function of zirconia content.

addition of 5 wt% ZrO_2 (5ZFA), the unit cell volume decreased. With increasing zirconia content to 10 wt%, the unit cell volume of FAp significantly expanded and reached a maximum after 5 h of milling (Fig. 4b). These variations in unit cell volume resulted mainly from increases in the (*a*) parameters, rather than from the (*c*) values and can probably be attributed to the ion exchange reaction (diffusion of larger ions of ZrO^{2+} into the FAp lattice) and lattice distortion of FAp during mechanical activation. Fig. 4c and d shows the deviations of lattice parameters and unit cell volume of FAp as a function of zirconia content. In the presence of 10 wt% ZrO_2, the lattice parameters and unit cell volume deviations of the FAp reached a maximum after 5 h of milling. Among the samples, 5ZFA specimen had the least deviation from the standard. So it can be concluded that the deviations of unit cell volume of FAp were significantly influenced by the zirconia content as follows:

$$10ZFA > 0ZFA > 5ZFA$$

3.3. Crystallite size and lattice strain

Fig. 5 shows the average crystallite size, lattice strain and volume fraction of grain boundary of specimens as a function of zirconia content. For 0ZFA, milling up to 5 h led to a rapid decrease in the crystallite size to less than 34 nm. In the presence of 5 wt% ZrO_2, a fine structure with an average crystallite size of about 29 nm was formed

(Fig. 5a). With increasing zirconia content to 10 wt%, the FAp crystallite size decreased and reached 24 nm after 5 h of milling. Conversely, the lattice strain and volume fraction of grain boundary of FAp enhanced with increasing zirconia content to 10 wt% (Fig. 5b and c). On the other side, the crystallite size of ZrO_2 declined with increasing zirconia content and reached 21 nm for 20ZFA (Fig. 5d). In opposition, with increasing the amount of zirconia to 20 wt%, the lattice strain and volume fraction of grain boundary of ZrO_2 intensified and reached 0.578 and 13%, respectively (Fig. 5e and f). It is obvious that the average crystallite sizes of FAp and ZrO_2 was influenced by the zirconia content as follows:

D_{FAp}: 0ZFA > 5ZFA > 10ZFA

D_{ZrO_2} : 5ZFA > 10ZFA > 15ZFA > 20ZFA

In accordance with the obtained results, the average crystallite size of FAp for 10ZFA was smaller than the other specimens due to the effect of added *m*-ZrO_2 on elevating lattice strain. The presence of *m*-ZrO_2 as second phase particles changes the local dislocation density distribution owing to strain incompatibility between the matrix and particles which may cause excessive accumulation of internal strain. This suggests the effect of the added second phase particles in accelerating grain size reduction which is in agreement with other references [10,17,18,].

3.4. Fraction of crystalline phase (crystallinity)

Fig. 6a shows the FWHM values at different Bragg angles for 0ZFA, 5ZFA and 10ZFA samples. The FWHM values illustrated the occurrence of anisotropic line broadening. It has been found that the anisotropic line broadening may be attributed to three factors: the presence of stacking faults, the presence of dislocations and nonequivalence of the grain sizes along different crystallographic directions [25]. Here, this phenomenon was presumably due to the grain size anisotropy. Fig. 6b displays the fraction of crystalline phase as a function of zirconia content. According to this figure, with increasing zirconia content, the crystallinity decreased and reached a minimum in the presence of 10 wt% ZrO_2. It is obvious that the fraction of crystallinity remarkably was influenced by the zirconia content as follows:

0ZFA > 5ZFA > 10ZFA

In general, control of the crystallinity of HAp is necessary for its biological applications. Since low crystallinity of calcium phosphates shows high osteoconductivity,

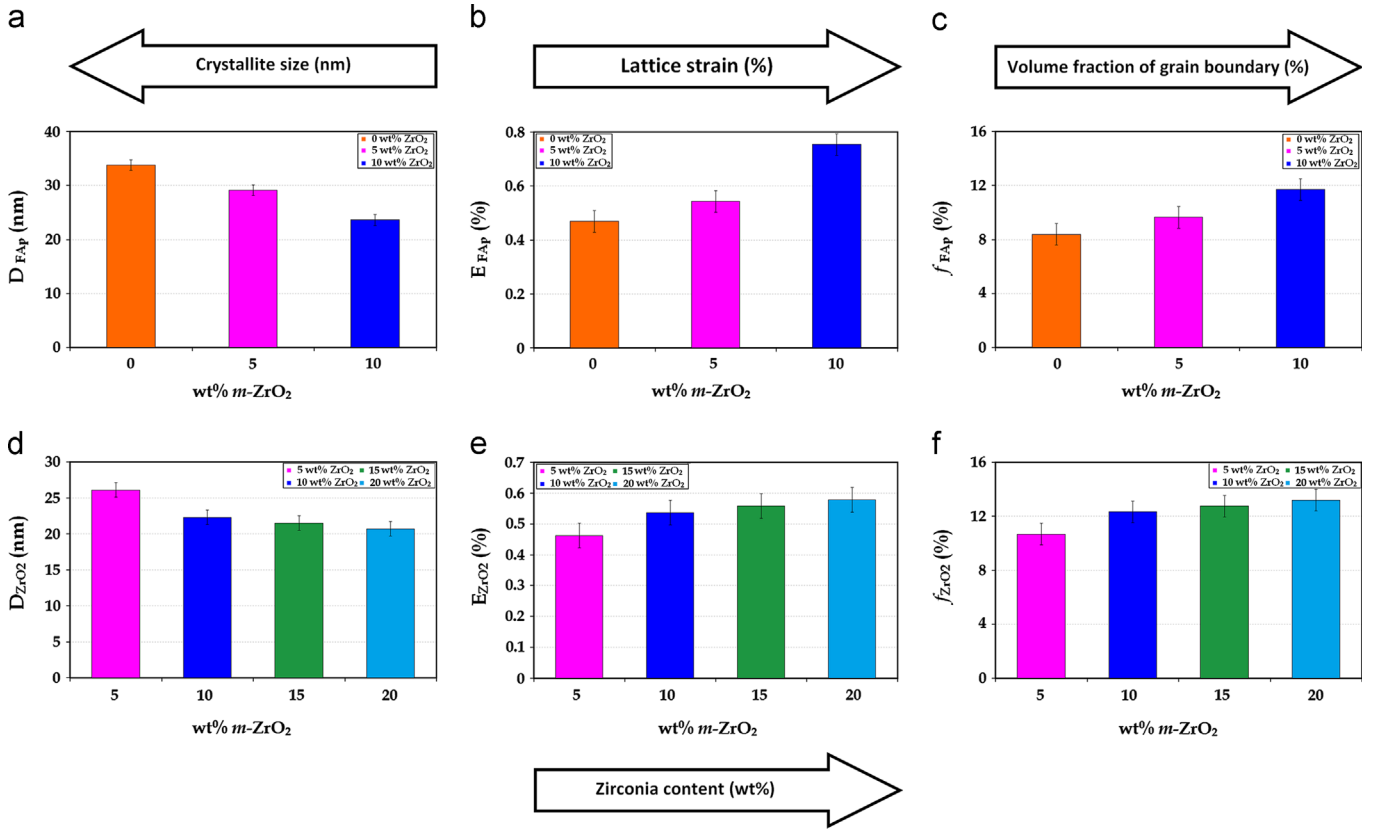

Fig. 5. Average crystallite size, lattice strain and volume fraction of grain boundary of specimens as a function of zirconia content (a,b,c) FAp and (d,e,f) *m*-ZrO_2.

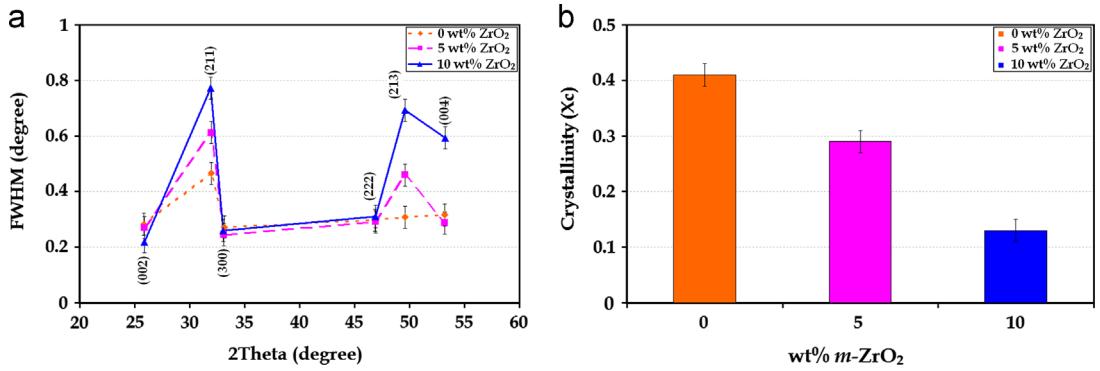

Fig. 6. (a) The FWHM values at different Bragg angles and (b) the fraction of crystalline phase as a function of zirconia content.

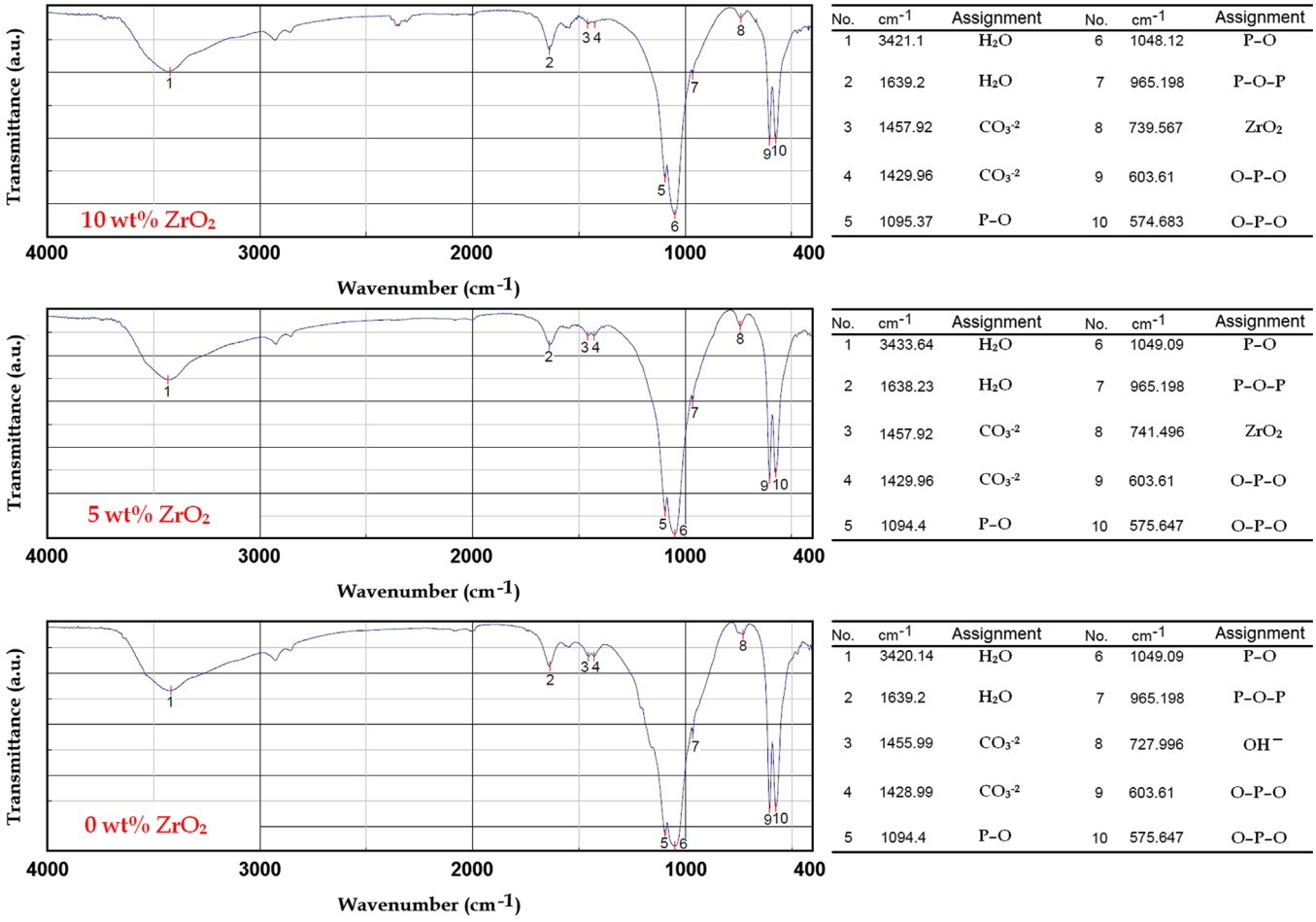

No.	cm^{-1}	Assignment	No.	cm^{-1}	Assignment
1	3421.1	H_2O	6	1048.12	P–O
2	1639.2	H_2O	7	965.198	P–O–P
3	1457.92	CO_3^{-2}	8	739.567	ZrO_2
4	1429.96	CO_3^{-2}	9	603.61	O–P–O
5	1095.37	P–O	10	574.683	O–P–O

No.	cm^{-1}	Assignment	No.	cm^{-1}	Assignment
1	3433.64	H_2O	6	1049.09	P–O
2	1638.23	H_2O	7	965.198	P–O–P
3	1457.92	CO_3^{-2}	8	741.496	ZrO_2
4	1429.96	CO_3^{-2}	9	603.61	O–P–O
5	1094.4	P–O	10	575.647	O–P–O

No.	cm^{-1}	Assignment	No.	cm^{-1}	Assignment
1	3420.14	H_2O	6	1049.09	P–O
2	1639.2	H_2O	7	965.198	P–O–P
3	1455.99	CO_3^{-2}	8	727.996	OH^-
4	1428.99	CO_3^{-2}	9	603.61	O–P–O
5	1094.4	P–O	10	575.647	O–P–O

Fig. 7. FT-IR spectra of the powder mixture in the absence and presence of different amounts of *m*-ZrO_2 (0–10 wt%).

the 5ZFA and 10ZFA samples can be used to promote osseointegration or as a coating to promote bone ingrowth in prosthetic implants [26].

3.5. FT-IR spectra

The FT-IR spectra of the 0ZFA, 5ZFA and 10ZFA specimens are shown in Fig. 7. The FT-IR analysis was used to get valid data about the functional group and to determine the composition of the samples in the absence and presence of different amounts of zirconia. The characteristic bands (listed in tables) exhibited in the 0ZFA, 5ZFA and 10ZFA spectra are assigned here:

(a) Two bands were observed at 3420 and 1639 cm^{-1} due to the vibration of the adsorbed water in the apatite structure [5]. These peaks shifted to 3433 and 1638 cm^{-1} for 5ZFA and 3421 and 1639 cm^{-1} for 10ZFA.
(b) In the absence of zirconia (0ZFA), the bands at 1094 and 1049 cm^{-1} arise from v_3 PO_4, the band at 965 cm^{-1}

results from v_1 PO_4, and the bands at 603 and 575 cm^{-1} result from v_1 PO_4 [5,17,18]. The phosphate bands in the 5ZFA and 10ZFA are slightly shifted compared to 0ZFA.

(c) For 0ZFA, a doublet appears at 1428 and 1455 cm^{-1} corresponding to ν_3 and a band at 864 cm^{-1} is attributed to v_2 vibration mode of the carbonated groups. These peaks shifted to 1429 and 1457 cm^{-1} for 5ZFA and 10ZFA respectively. The presence of these peaks showed that FAp and FAp in the composites contained some CO_3^{2-} groups in PO_4^{3-} sites of apatite lattice (B-type substitution) [27]. It has been reported that this kind of apatite is more similar to biological apatite and could be more suitable for bone replacement materials [5].

(d) Also, for 0ZFA, the band at 727 cm^{-1} corresponds to the shifting OH^- liberation mode. This is caused by the increase of F^- content in the (OH^-, F^-) chain of apatite with predominant configuration of …FHO:OHF… [28]. It has been found that this configuration is typical for samples in which almost 50% of OH^- ions is being replaced by F^- ions. Besides the band at 727 cm^{-1}, appearance of the band at 758 cm^{-1} shows that the configuration …FHOF… is predominant [28]. It should be mentioned that for 5ZFA and 10ZFA, these bands overlapped with the band corresponding to the vibration of ZrO_2. For 5ZFA, the band at 741 cm^{-1} is attributed to the vibration of ZrO_2 which shifted to 739 cm^{-1} with increasing zirconia content up to 10 wt% (10ZFA).

The FT-IR findings suggest that the formation of fluorapatite–zirconia composite nanopowders was influenced by the zirconia content.

3.6. Elemental analysis

Fig. 8 displays the EDX spectra of the CaO, P_2O_5 and CaF_2 powder mixture in the absence and presence of different amounts of *m*-ZrO_2 (0–20 wt%) after mechanical activation for 5 h. According to EDX spectra, the main elements of the specimens were calcium, phosphorus, oxygen, fluorine and zirconium. The EDX spectra of the 0ZFA, 5ZFA, 10ZFA, 15ZFA and 20ZFA showed a molar ratio of Ca/P = 1.83, 1.72, 1.74, 1.91 and 1.81, respectively. As expected, with increasing zirconia content the relative intensity of ZrO_2 was dominant. Results confirmed that a very homogeneous distribution of components was formed after mechanical activation for 5 h, specifically for the 5ZFA and 10ZFA. At about 0ZFA, 15ZFA and 20ZFA, the increase in Ca/P ratio to more than 1.67 may be ascribed to the formation of calcium phosphate compounds with lower Ca/P ratio than 1.67 which is in agreement with previous research [29]. Furthermore, EDX point chemical analysis revealed that no chemically stable contaminants were detected due to the excessive adhesion of powders to the milling media. Based on our experiments, polymeric vial is an appropriate milling media to annihilate contamination problem and to achieve modified morphologies with high biomedical performance [6,17–19,30].

3.7. SEM/FE-SEM observations

Fig. 9 shows the SEM images of all the samples in the absence and presence of different amounts of *m*-ZrO_2 (0–20 wt%) after mechanical activation for 5 h. According to this figure, the gained powders showed cluster-like structures which were composed of several fine particles. By adding 5 wt% *m*-ZrO_2 to powder mixture, the rate of fracturing increased and as a result the size of powder particles decreased. For 5ZFA, the morphology of nanoparticles was almost equiaxed with the average size of about 45 nm. With increasing zirconia content to 10 wt%, the equiaxed particles exhibited an average size of about 40 nm. Further increasing zirconia content to 20 wt%, resulted in the formation of large polygonal agglomerates/particles. Based on SEM images, no significant changes in the size distribution and morphology of the agglomerates were observed. However, in accordance with higher magnification images, the samples with 5 and 10 wt% *m*-ZrO_2 had fine homogeneous microstructures.

In this paper, FE-SEM images were used to appraise the volume fraction of grain boundary of the nanopowders by using the edge mode images. Fig. 10 displays the edge mode images of the 0ZFA, 5ZFA and 10ZFA after 5 h of milling. According to this micrograph, the volume fraction of grain boundary in 10ZFA sample is higher than in other specimens. This suggests that the average particle size of 10ZFA is lower than that of other samples. As a result, the addition of appropriate amount of zirconia as a second phase in calcium phosphate-based composites acts as a driving force to increase the volume fraction of grain boundary. The gained result is consistent with the presented data in the section of crystallite size and lattice strain. Recalling from the above consequences, it can be concluded that the mechanosynthesis of FAp–ZrO_2 composite nanopowders was influenced by the zirconia content. Also, in comparison with other specimens, the 5ZFA and 10ZFA samples had appropriate structural features and morphological characteristics which can be considered for particular targets.

4. Conclusions

The effect of zirconia content on the mechanochemical synthesis and structural features of fluorapatite–zirconia composite nanopowders was investigated. After 5 h of milling, the main products of mechanochemical reactions for 5 and 10 wt% zirconia were FAp–5 wt% ZrO_2 and FAp–10 wt% ZrO_2 composites, respectively. With increasing zirconia content up to $\geq$ 15 wt%, there was no trace of fluorapatite–zirconia composite due to the stabilization of *m*-ZrO_2 by calcium fluoride and calcium oxide as well as

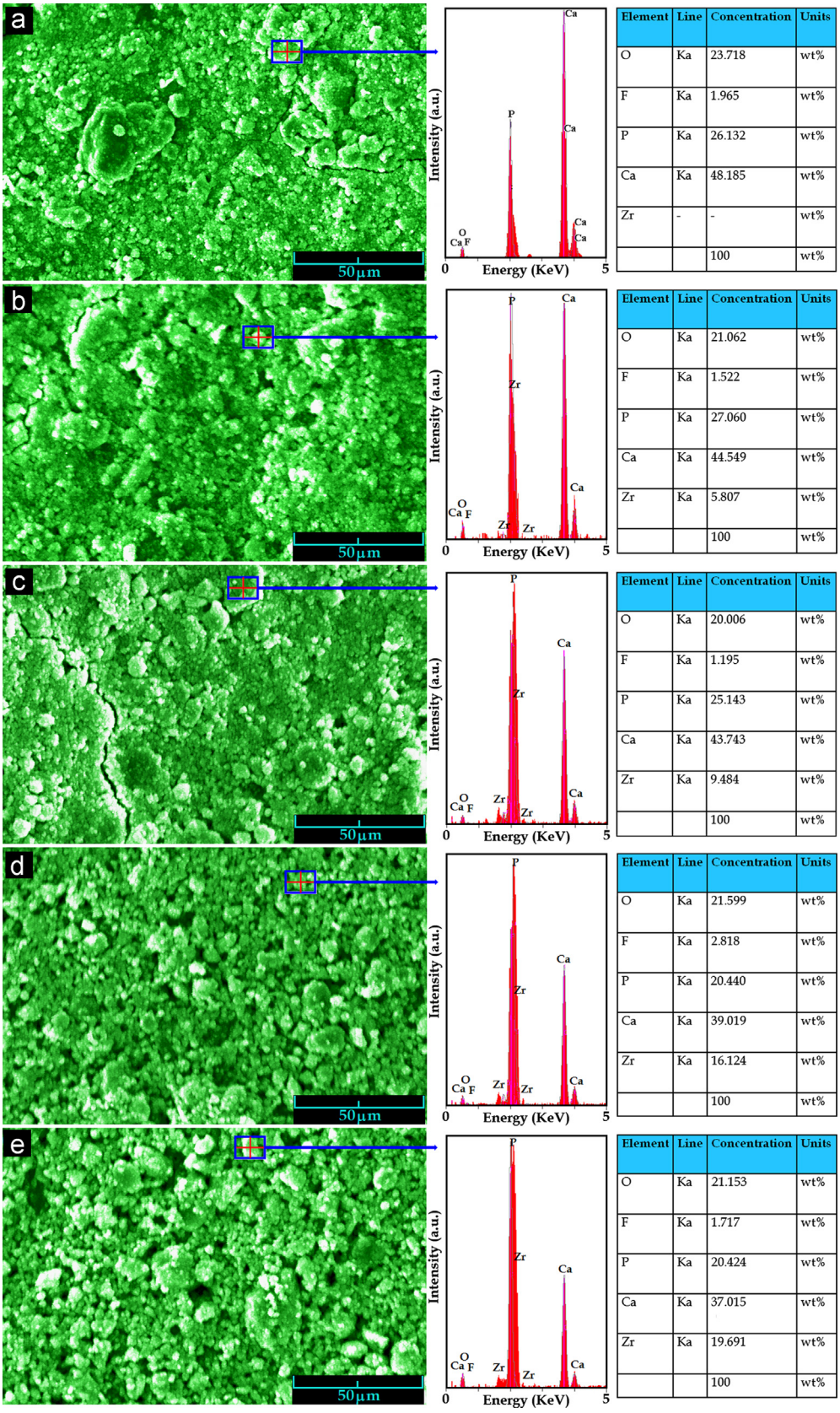

Fig. 8. EDX spectra of the CaO, P_2O_5 and CaF_2 powder mixture (a) in the absence and presence of different amounts of *m*-ZrO_2 (b) 5, (c) 10, (d) 15 and (e) 20 wt% after mechanical activation for 5 h.

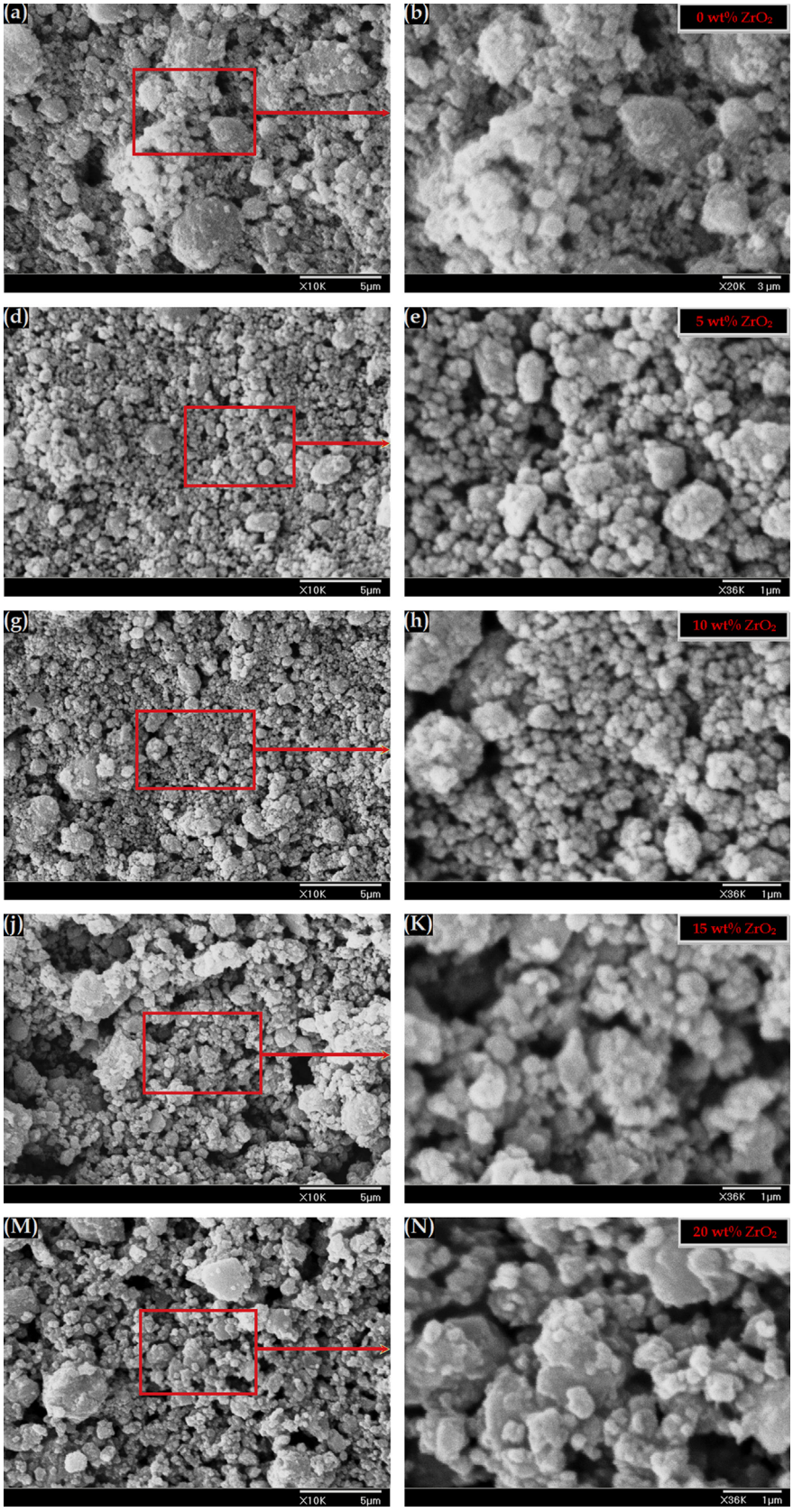

Fig. 9. SEM images of all the samples in the (a) absence and presence of different amounts of m-ZrO_2 (b) 5, (c) 10, (d) 15 and (e) 20 wt% after mechanical activation for 5 h.

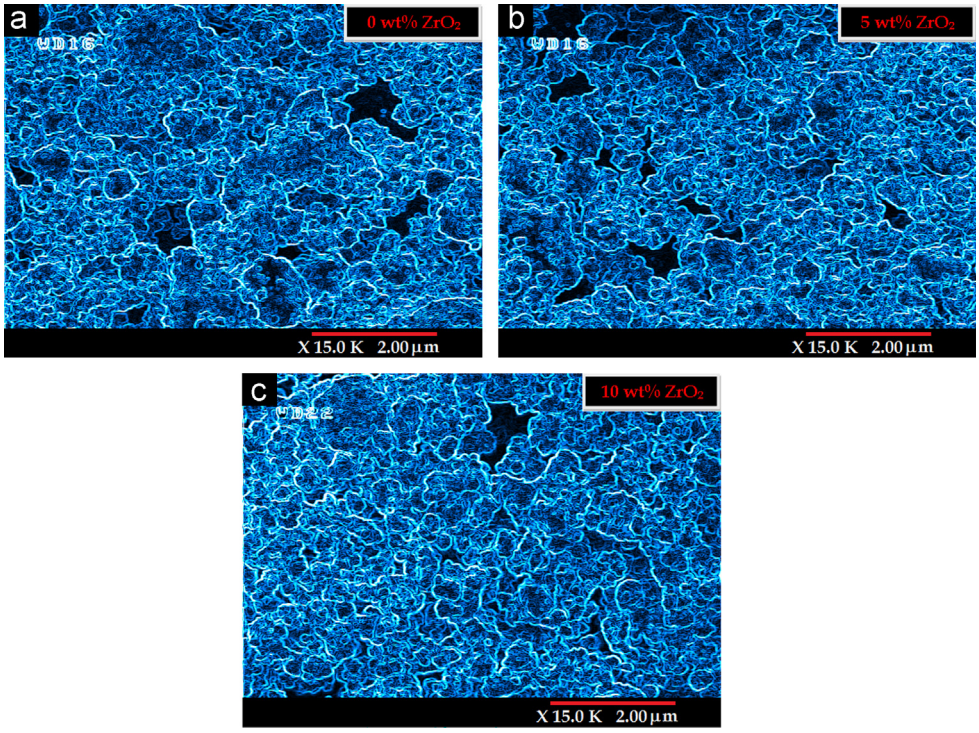

Fig. 10. FE-SEM edge mode images of the (a) 0ZFA, (b) 5ZFA and (c) 10ZFA after 5 h of milling.

the formation of a solid solution. With increasing zirconia content to 10 wt%, the unit cell volume of FAp significantly expanded and reached a maximum after 5 h of milling. Results revealed that the deviations of unit cell volume of FAp were significantly influenced by the zirconia content. The average crystallite size of FAp in the composite structures was smaller than the single phase FAp. By increasing zirconia content, the crystallinity decreased and reached a minimum in the presence of 10 wt% ZrO_2. EDX results confirmed that a very homogeneous distribution of components was formed after mechanical activation for 5 h. FE-SEM images suggest that addition of appropriate amount of zirconia to calcium phosphate-based composites acts as a driving force to increase the volume fraction of grain boundary.

Acknowledgment

The authors are grateful to research affairs of Islamic Azad University, Najafabad Branch for supporting of this research.

References

[1] M. Okada, T. Furuzono, Hydroxylapatite nanoparticles: fabrication methods and medical applications, Science and Technology of Advanced Materials 13 (2012) 1–14.
[2] S.J. Kalita, A. Bhardwaj, H.A. Bhatt, Nanocrystalline calcium phosphate ceramics in biomedical engineering, Materials Science and Engineering C 27 (2007) 441–449.
[3] M. Fini, L. Savarino, N.N. Aldini, L. Martini, G. Giavaresi, G. Rizzi, D. Martini, A. Ruggeri, A. Giunti, R. Giardino, Biomechanical and histomorphometric investigations on two morphologically differing titanium surfaces with and without fluorohydroxyapatite coating: an experimental study in sheep tibiae, Biomaterials 24 (2003) 3183–3192.
[4] Y. Chen, X. Miao, Thermal and chemical stability of fluorohydroxyapatite ceramics with different fluorine contents, Biomaterials 26 (2005) 1205–1210.
[5] M.H. Fathi, E. Mohammadi Zahrani, Mechanical alloying synthesis and bioactivity evaluation of nanocrystalline fluoridated hydroxyapatite, Journal of Crystal Growth 311 (2009) 1392–1403.
[6] R. Ebrahimi-Kahrizsangi, B. Nasiri-Tabrizi, A. Chami, Characterization of single-crystal fluorapatite nanoparticles synthesized via mechanochemical method, Particuology 9 (2011) 537–544.
[7] B. Viswanath, N. Ravishankar, Interfacial reactions in hydroxyapatite/alumina nanocomposites, Scripta Materialia 55 (2006) 863–866.
[8] R.R. Rao, T.S. Kannan, Synthesis and sintering of hydroxyapatite–zirconia composites, Materials Science and Engineering C 20 (2002) 187–193.
[9] F. Ben Ayed, J. Bouaziz, Sintering of tricalcium phosphate–fluorapatite composites with zirconia, Journal of the European Ceramic Society 28 (2008) 1995–2002.
[10] Z. Evis, Reactions in hydroxylapatite–zirconia composites, Ceramics International 33 (2007) 987–991.
[11] C.C. Silva, M.A. Valente, M.P.F. Graça, A.S.B. Sombra, Preparation and optical characterization of hydroxyapatite and ceramic systems with titanium and zirconium formed by dry high-energy mechanical alloying, Solid State Sciences 6 (2004) 1365–1374.
[12] S. Nath, R. Tripathi, B. Basu, Understanding phase stability, microstructure development and biocompatibility in calcium phosphate–titania composites, synthesized from hydroxyapatite and titanium powder mixture, Materials Science and Engineering C 29 (2009) 97–107.
[13] H.W. Kim, Y.M. Kong, Y.H. Koh, H.E. Kim, Pressureless sintering and mechanical and biological properties of fluor-hydroxyapatite composites with zirconia, Journal of the American Ceramic Society 86 (2003) 2019–2026.
[14] J.-W. Choi, Y.-M. Kong, H.-E. Kim, I.-S. Lee, Reinforcement of hydroxyapatite bioceramic by addition of Ni_3Al and Al_2O_3, Journal of the American Ceramic Society 81 (1998) 1743–1748.

[15] Z. Evis, R.H. Doremus, Hot-pressed hydroxylapatite/monoclinic zirconia composites with improved mechanical properties, Journal of Materials Science 42 (2007) 2426–2431.
[16] Z. Evis, M. Usta, I. Kutbay, Hydroxyapatite and zirconia composites: effect of MgO and MgF_2 on the stability of phases and sinterability, Materials Chemistry and Physics 110 (2008) 68–75.
[17] B. Nasiri-Tabrizi, A. Fahami, Synthesis and characterization of fluorapatite–zirconia composite nanopowders, Ceramics International (2012) http://dx.doi.org/10.1016/j.ceramint.2012.11.016.
[18] B. Nasiri-Tabrizi, A. Fahami, Reaction mechanisms of synthesis and decomposition of fluorapatite–zirconia composite nanopowders, Ceramics International (2012) http://dx.doi.org/10.1016/j.ceramint.2012.12.008.
[19] A. Fahami, B. Nasiri-Tabrizi, R. Ebrahimi-Kahrizsangi, Synthesis of calcium phosphate-based composite nanopowders by mechanochemical process and subsequent thermal treatment, Ceramics International 38 (2012) 6729–6738.
[20] F. Sun, F.H.S. Froes, Synthesis and characterization of mechanical-alloyed Ti_xMg alloys, Journal of Alloys and Compounds 340 (2002) 220–225.
[21] J. Qian, Y. Kang, W. Zhang, Z. Li, Fabrication, chemical composition change and phase evolution of biomorphic hydroxyapatite, Journal of Materials Science: Materials in Medicine 19 (2008) 3373–3383.
[22] W.F. Smith, J. Hashemi, Foundations of Materials Science and Engineering, Crystal Structures and Crystal Geometry, McGraw-Hill Science, New York, 2004, pp. 67–115.
[23] Z. Wei, T. Xia, J. Ma, W. Feng, J. Dai, Q. Wang, P. Yan, Investigation of the lattice expansion for Ni nanoparticles, Materials Characterization 58 (2007) 1019–1024.
[24] E. Landi, A. Tampieri, G. Celotti, S. Sprio, Densification behavior and mechanisms of synthetic hydroxyapatites, Journal of the European Ceramic Society 20 (2000) 2377–2387.
[25] M.M. Seckler, M. Danese, S. Derenzo, J.V. Valarelli, M. Giulietti, R. Rodriguez-Clemente, Influence of process conditions on hydroxyapatite crystallinity obtained by direct crystallization, Journal of Materials Research 2 (1999) 59–62.
[26] K.P. Sanosh, M.C. Chu, A. Balakrishnan, Y.J. Lee, T.N. Kim, S.J. Cho, Synthesis of nano hydroxyapatite powder that simulate teeth particle morphology and composition, Current Applied Physics 9 (2009) 1459–1462.
[27] J.P. Lafon, E. Champion, D. Bernache-Assollant, Processing of AB-type carbonated hydroxyapatite $Ca_{10-x}(PO_4)_{6-x}(CO_3)_x(OH)_{2-x-2y}(CO_3)_y$ ceramics with controlled composition, Journal of the European Ceramic Society 28 (2008) 139–147.
[28] I. Nikcevic, V. Jokanovic, M. Mitric, Z. Nedic, D. Makovec, D. Uskokovic, Mechanochemical synthesis of nanostructured fluorapatite/fluorhydroxyapatite and carbonated fluorapatite/fluorhydroxyapatite, Journal of Solid State Chemistry 177 (2004) 2565–2574.
[29] M. Kitamura, Ch. Ohtsuki, Sh.I. Ogata, M. Kamitakahara, M. Tanihara, Microstructure and bioresorbable properties of α-TCP ceramic porous body fabricated by direct casting method, Materials Transactions 45 (2004) 983–988.
[30] B. Nasiri-Tabrizi, P. Honarmandi, R. Ebrahimi-Kahrizsangi, P. Honarmandi, Synthesis of nanosize single-crystal hydroxyapatite via mechanochemical method, Materials Letters 63 (2009) 543–546.